

Mitigation of Low-Frequency Current Ripple in Fuel-Cell Inverter Systems Through Waveform Control

Guo-Rong Zhu, *Member, IEEE*, Siew-Chong Tan, *Senior Member, IEEE*, Yu Chen, *Member, IEEE*, and Chi K. Tse, *Fellow, IEEE*

Abstract—Fuel-cell power systems comprising single-phase dc/ac inverters draw low-frequency ac ripple currents at twice the output frequency from the fuel cell. Such a 100/120 Hz ripple current may create instability in the fuel-cell system, lower its efficiency, and shorten the lifetime of a fuel cell stack. This paper presents a waveform control method that can mitigate such a low-frequency ripple current being drawn from the fuel cell while the fuel-cell system delivers ac power to the load through a differential inverter. This is possible because with the proposed solution, the pulsation component (cause of ac ripple current) of the output ac power will be supplied mainly by the two output capacitors of the differential inverter while the average dc output power is supplied by the fuel cell. Theoretical analysis, simulation, and experimental results are provided to explain the operation and showcase the performance of the approach. Results validate that the proposed solution can achieve significant mitigation of the current ripple as well as high-quality output voltage without extra hardware. Application of the solution is targeted at systems where current ripple mitigation is required, such as for the purpose of eliminating electrolytic capacitor in photovoltaic and LED systems.

Index Terms—Active method, decouple, fuel cell, low-frequency current ripple, pulsation power, waveform control.

I. INTRODUCTION

THE conversion of dc power into ac power through a single-phase inverter will typically introduce a low-frequency current ripple (at twice the ac output voltage frequency) at the

Manuscript received February 9, 2012; revised April 22, 2012; accepted May 28, 2012. Date of current version September 27, 2012. This work was supported in part by the National Natural Science Foundation of China under Grant 51107092, in part by the University Grants Committee of the Hong Kong Special Administrative Region, in part by the Research Grants Council Earmarked Research Grant PolyU 5283/08E, in part by the China Postdoctoral Science Foundation under Project 2012M511693, and in part by the Fundamental Research Funds for the Central Universities of China under Grant 2011-IV-117. Recommended for publication by Associate Editor J. Choi.

G.-R. Zhu is with the School of Automation, Wuhan University of Technology, Wuhan, Hubei 430070, China (e-mail: zhgr_55@hotmail.com).

S.-C. Tan is with the Department of Electrical and Electronic Engineering, The University of Hong Kong, Pokfulam, Hong Kong (e-mail: sctan@hku.hk).

Y. Chen is with the College of Electrical and Electronic Engineering, Huazhong University of Science and Technology, Wuhan, Hubei 430074, China (e-mail: ayu03@163.com).

C. K. Tse is with the Department of Electronic and Information Engineering, The Hong Kong Polytechnic University, Hung Hom, Kowloon, Hong Kong (e-mail: encktse@polyu.edu.hk).

Color versions of one or more of the figures in this paper are available online at <http://ieeexplore.ieee.org>.

Digital Object Identifier 10.1109/TPEL.2012.2205407

dc input side of the power conversion system. In a typical 50-Hz or 60-Hz single-phase inverter system, the ripple is, respectively, 100 and 120 Hz [2]. The presence of such a ripple is detrimental and damaging to a dc source made up of fuel cells. As pointed out in [2]–[8], the various disadvantages include: 1) significant wastage in fuel consumption [2], [3]; 2) oxygen starvation leading to reduced maximum power generation [4], [5]; 3) poor dynamic response [6]; 4) nuisance tripping at heavy load [7]; and 5) shortening of fuel cell's lifetime [4], [8].

For this reason, the issues and standards concerning the limitation of the low-frequency current ripple are often specified in technical reports and manufacturers' manuals [9], [10]. According to [9], it is recommended that the 100/120 Hz ripple component be limited to within 15% of the total output and the 60 Hz ripple component be limited to within 10% at 10–100% loads for an overall improved efficiency and fuel cell's lifetime. The Ballard Nexa 1.2-kW PEMFC is set to a 120 Hz current ripple limit of up to 35% of the peak-to-peak value, or up to 24.7% of the root mean square (rms) value [10]. Consequently, the subject of mitigating low-frequency input current ripple of inverters has become an important topic in fuel-cell power system research.

In particular, various passive energy storage compensation methods have been proposed in [11], which involve the incorporation of a large dc capacitor, passive-resonant circuit, or battery at the dc line. The drawback of this approach is that the product size and cost will be increased. Alternative solutions involving active harmonic filter compensation using an external converter were also proposed to mitigate the low-frequency current ripple [12]–[21]. While these methods are feasible, they also require extra hardware and are typically not preferred.

On the other hand, it is also possible to mitigate the current ripple through the use of active control methods, e.g., by using a dual-loop control [1] or by using a moving-average filter [22]. These methods do not incur extra component cost and can reduce the low-frequency ripple during steady state, thereby allowing the reduction of the storage capacitance. However, these methods can achieve only partial mitigation of the low-frequency ripple and generate large overshoots during load transients, which will induce oscillation that will lead to slow dynamic response at the dc bus.

In this paper, an approach of mitigating low-frequency current ripple of fuel-cell power systems through the application of waveform control on differential power inverters is proposed.

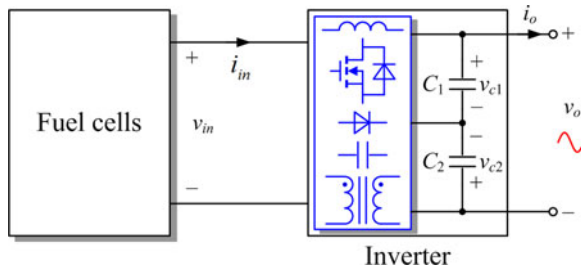


Fig. 1. Diagram of a fuel cell with a differential inverter.

A comparative study on the proposed waveform control and the traditional control method without waveform control used in [20] and [21], under the same topology, is performed. It will be clearly illustrated in this paper that the proposed solution achieves significant suppression of the low-frequency current ripple without any additional component, circuit, or electrolytic capacitor, therefore maintaining the overall size and cost. Additionally, the current stress of the switch is decreased and the total efficiency is improved with the use of waveform control.

II. FUEL-CELL SYSTEMS BASED ON DIFFERENTIAL INVERTERS

A. Overview

Differential inverters have been widely applied to ac applications powered by dc sources, e.g., in fuel-cell inverter systems, due to its advantages of high efficiency, reduced size, and low cost [23]–[30]. Fig. 1 shows a diagram of a fuel-cell system with a differential inverter. Here, v_{in} and i_{in} , respectively, represent the input voltage and current of the differential inverter, which is also the output voltage and current of the fuel cell. The output voltage and current of the inverter, which are both ac sinusoidal quantities, are depicted as v_o and i_o , respectively. v_o is the difference of v_{c1} and v_{c2} , which are the voltages of the inverter's output capacitors C_1 and C_2 , respectively.

B. Analysis

A differential inverter is an inverter made up of two identical bidirectional dc/dc (i.e., buck, boost, or buck–boost) converters to deliver in a single stage, either a boost, a buck, or a buck–boost operation together with the voltage inverter function. Based upon the dc/dc converter type, each converter will generate a dc-biased ac output voltage that is higher or lower than the fuel cells voltage of which when the outputs of the two dc/dc converters are combined, only a pure ac output voltage is generated. In conventional practice, a voltage control will be applied on the respective converter to ensure that the output voltage of each converter and their combined output voltage will be, respectively

$$v_{c1} = V_d + \frac{1}{2}V_{max} \sin(\omega t) \quad (1)$$

$$v_{c2} = V_d + \frac{1}{2}V_{max} \sin(\omega t - \pi) \quad (2)$$

and

$$v_o = v_{c1} - v_{c2} = V_{max} \sin(\omega t) \quad (3)$$

where v_{c1} and v_{c2} are the output voltages of the two dc/dc converters, V_{max} is the amplitude of the output voltage v_o , ω is the line frequency, and V_d is the dc-biased voltage of v_{c1} and v_{c2} . From (3), it can be observed that the required output is as desired, i.e., comprising only the ac component.

For a single-phase inverter system operating with unity power factor, the ideal output current can be written as

$$i_o = I_{max} \sin(\omega t) \quad (4)$$

where I_{max} is the amplitude of the output current i_o .

Multiplying (3) with (4) gives the output power p_o as

$$p_o = \frac{1}{2}V_{max}I_{max}(1 - \cos(2\omega t)). \quad (5)$$

The double-line-frequency component of the power is reflected in the $\cos(2\omega t)$ term. On the other hand, the output power of the fuel cell can be expressed as

$$p_{dc} = V_{in}(I_{indc} + i_{inac}) \quad (6)$$

where I_{indc} and i_{inac} are the dc and ac components of the current, respectively. Assuming 100% power efficiency and that the fuel-cell voltage is constant, I_{indc} will be

$$I_{indc} = \frac{V_{max}I_{max}}{2V_{in}}. \quad (7)$$

From (5)–(7), the ac component i_{inac} is

$$i_{inac} = \frac{V_{max}I_{max}}{2V_{in}} \cos(2\omega t). \quad (8)$$

As given in (8), the $2\omega t$ ripple current drawn from the fuel cell can be significant if no capacitor is installed at the dc side to provide energy buffering. Fig. 2(a) shows the waveforms of a differential inverter operating with unity power factor as described in this section.

C. Altering of the Waveforms of a Differential Inverter

From (3), it can be seen that it is possible to individually control the output voltages of the dc/dc converters of the differential inverter, i.e., v_{c1} and v_{c2} , such that they differ from (1) and (2), while still maintaining a pure sinusoidal output voltage v_o . For example, the component $F(t)$ can be added to (1) and (2) to give

$$v_{c1} = V_d + \frac{1}{2}V_{max} \sin(\omega t) + F(t) \quad (9)$$

and

$$v_{c2} = V_d + \frac{1}{2}V_{max} \sin(\omega t - \pi) + F(t). \quad (10)$$

However, $v_o = v_{c1} - v_{c2} = V_{max} \sin(\omega t)$ will still be equivalent to (3). The ability to alter v_{c1} and v_{c2} brought up the question as to whether the adding of such compensating components can mitigate the input current ripple given in (8) and shown in Fig. 2(a). We found that this is hypothetically possible. If v_{c1} and v_{c2} are controlled such that they behave the way as shown

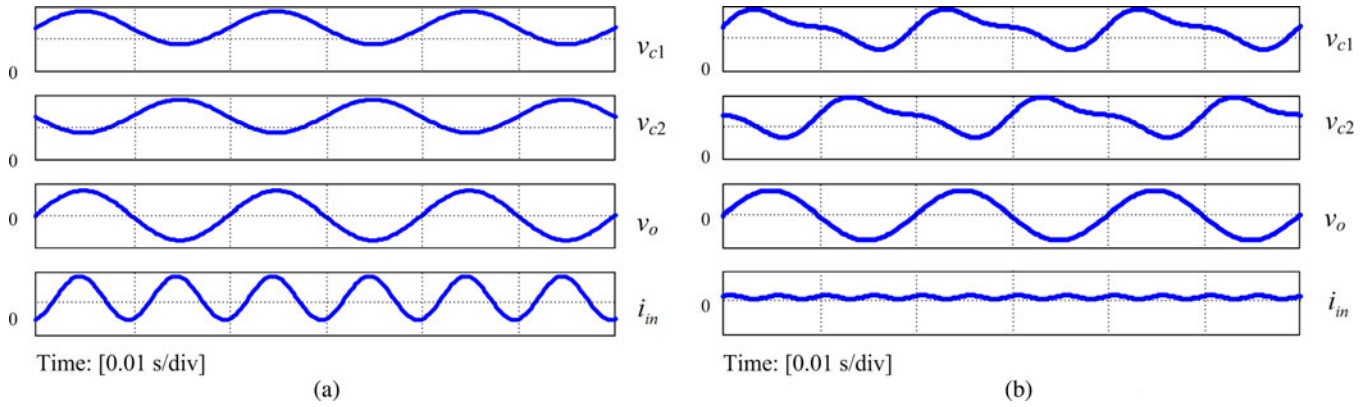


Fig. 2. Waveforms of a differential inverter operating with unity power factor (a) without waveform control and (b) with waveform control.

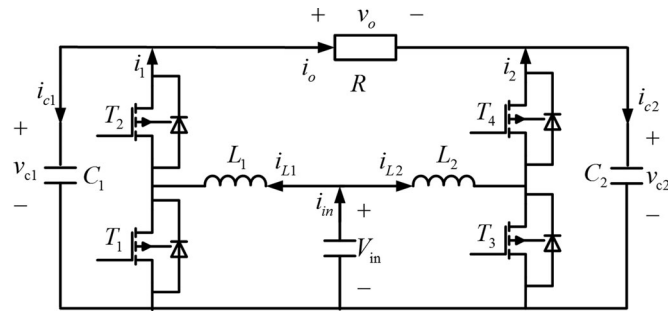


Fig. 3. Schematic of the boost-type differential inverter.

in Fig. 2(b), the input current ripple will be reduced. This is the so-called waveform control method proposed in this paper.

III. PROPOSED WAVEFORM CONTROL METHOD

In this paper, a boost-type differential inverter made up of two bidirectional boost converters (see Fig. 3) is adopted as the case study example in the fuel-cell system for describing the proposed waveform control. Here, V_{in} is the dc input voltage, L_1 and L_2 are the power inductors, T_1 – T_4 are the power switches, D_1 and D_2 are the free-wheeling diodes, C_1 and C_2 are the output capacitors, and R is the load resistance.

If the capacitor voltages of the two boost converters can be, respectively, controlled as

$$v_{c1} = V_d + \frac{1}{2}V_{\max} \sin(\omega t) + B \sin(2\omega t + \varphi) \quad (11)$$

and

$$v_{c2} = V_d + \frac{1}{2}V_{\max} \sin(\omega t - \pi) + B \sin(2\omega t + \varphi) \quad (12)$$

then v_o will be equivalent to (3). The objective of the waveform control method is to ensure that the capacitor voltages follow precisely (11) and (12). According to [31], to maximize the efficiency of the converter, the minimum dc bias for the converters is

$$V_d > \frac{1}{2}V_{\max} + V_{in} + B. \quad (13)$$

Since $i = C \frac{dV}{dt}$, the currents of capacitors C_1 and C_2 (for $C = C_1 = C_2$) can be found from (11) and (12) as

$$i_{c1} = C\omega \frac{1}{2}V_{\max} \cos(\omega t) + 2C\omega B \cos(2\omega t + \varphi) \quad (14)$$

and

$$i_{c2} = -C\omega \frac{1}{2}V_{\max} \cos(\omega t) + 2C\omega B \cos(2\omega t + \varphi). \quad (15)$$

Accordingly, from Fig. 3

$$i_1 = i_o + i_{c1} = I_{\max} \sin(\omega t) + C\omega \frac{1}{2}V_{\max} \cos(\omega t) + 2C\omega B \cos(2\omega t + \varphi) \quad (16)$$

$$i_2 = -i_o + i_{c2} = -I_{\max} \sin(\omega t) - C\omega \frac{1}{2}V_{\max} \cos(\omega t) + 2C\omega B \cos(2\omega t + \varphi). \quad (17)$$

Then, the inductor currents will be

$$i_{L1} = \frac{i_1}{1 - d_1} = \frac{i_1 v_{c1}}{v_{in}} \quad (18)$$

and

$$i_{L2} = \frac{i_2}{1 - d_2} = \frac{i_2 v_{c2}}{v_{in}} \quad (19)$$

where d_1 and d_2 are, respectively, the duty cycles of T_1 and T_3 . Therefore, the input current of the inverter, which is the sum of i_{L1} and i_{L2} , will be

$$i_{in} = \frac{V_{\max} I_{\max} + 2B^2 C\omega \sin(4\omega t + \varphi) - V_{\max} I_{\max} \cos(2\omega t)}{2V_{in}} + \frac{\frac{1}{2}V_{\max}^2 \omega C \sin(2\omega t) + 8V_d B C\omega \cos(2\omega t + \varphi)}{2V_{in}}. \quad (20)$$

From (20), there are three components in the input current i_{in} . They are the dc part $\frac{V_{\max} I_{\max}}{2V_{in}}$ which is identical to (7), the component at 4ω which is $\frac{2B^2 C\omega \sin(4\omega t + \varphi)}{2V_{in}}$, and the low-frequency component at 2ω which is

$$i_{in(2\omega)} = \frac{-V_{\max} I_{\max} \cos(2\omega t) + \frac{1}{2}V_{\max}^2 \omega C \sin(2\omega t)}{2V_{in}} + \frac{8V_d B C\omega \cos(2\omega t + \varphi)}{2V_{in}}. \quad (21)$$

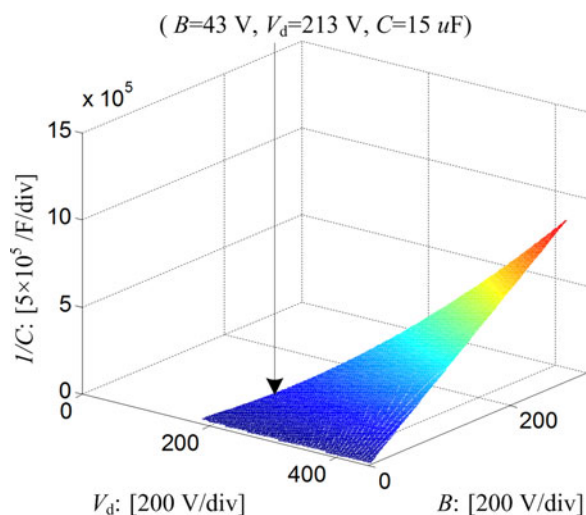


Fig. 4. 3-D plot of the relationship of B , V_d , and C .

From (21), it can be seen that if we set

$$-V_{\max} I_{\max} \cos(2\omega t) + \frac{1}{2} V_{\max}^2 \omega C \sin(2\omega t) + 8V_d B C \omega \cos(2\omega t + \varphi) = 0 \quad (22)$$

then $i_{in(2\omega)} = 0$. This means that there will not be a 2ω component in the input current i_{in} . From (22), amplitude B is derived as

$$B = \frac{V_{\max}}{8V_d \omega C} \sqrt{I_{\max}^2 + \omega^2 C^2 V_{\max}^2 / 4} \quad (23)$$

and the phase angle φ is derived as

$$\varphi = \frac{\pi}{2} - \sin^{-1} \frac{I_{\max}}{\sqrt{I_{\max}^2 + \omega^2 C^2 V_{\max}^2 / 4}} \quad (24)$$

By ensuring that the capacitor voltages track precisely (11) and (12), of which B and φ are calculated from (23) and (24), the low-frequency current ripple of the inverter will be mitigated.

IV. ANALYSIS ON THE WAVEFORM CONTROL METHOD

A. Characteristics of Waveform Control

According to (23), the capacitor C and its dc offset voltage V_d are inversely proportional to B . At the same time, V_d and B should satisfy the inequality given in (13). Additionally, with the boost differential inverter, a large amplitude of V_d and B would mean a big duty cycle, which may lead the converter to operate at the saturation region of the duty cycle. The size of C is also an important factor that will increase the overall size and cost of the system. Thus, with all these constraints in mind, the three parameters must be optimized and designed accordingly to the application.

Fig. 4 shows a 3-D plot of the relationship of C , V_d , and B calculated with $P_o = 170$ W at $f = 50$ Hz and $V_{\max} = \sqrt{2} \times 110$ V using (23). It can be seen that $C = 15$ μ F, $V_d = 213$ V, and $B = 43$ V. According to (24), it can be calculated that $\varphi = 0.1659$. Thus, $v_{c1} =$

$$213 + 77.75 \sin(\omega t) + 43 \sin(2\omega t + 0.1659) \text{ and } v_{c2} = 213 - 77.75 \sin(\omega t) + 43 \sin(2\omega t + 0.1659).$$

Fig. 5(a)–(f) shows the simulated operating waveforms of the boost inverter with a sinusoidal ac output voltage.

Fig. 5(a) and (d) shows, respectively, the waveforms of the duty cycle signal without waveform control and with the proposed waveform control, where d_1 and d_2 are the duty cycles of the two bidirectional boost converters. From the figures, it can be seen that the output voltage is zero at approximately $d_1 = d_2 = 0.58$. The range of d_1 and d_2 for the boost inverter without waveform control is 0.33–0.69 and that with waveform control is 0.15–0.7. Both ranges are well within the practical limits of the boost converter.

Fig. 5(b) and (e) shows the waveforms of v_{c1} , v_{c2} , and v_o of the boost differential inverter without waveform control and with waveform control, respectively. It can be seen that the output voltage v_o is sinusoidal in both cases even though in the case of waveform control, v_{c1} and v_{c2} are distorted with a double-line-frequency component.

Fig. 5(c) and (f) shows the waveforms of i_{L1} , i_{L2} , and i_{in} of the inverter without waveform control and with waveform control, respectively. In the case of no waveform control, the input current i_{in} contains a high level of double-line-frequency ripple. Conversely, with the proposed waveform control, the ripple of the input current is significantly mitigated. The ripple is at four times the line frequency and the amplitude is reduced to less than 10% of that without waveform control, from 3.8 to 0.38 A_{rms} .

B. Voltage and Current Stresses With Waveform Control

The maximum capacitor voltage of the inverter with the waveform control is $v_{c1 \max} = v_{c2 \max} = 314$ V [see Fig. 5(e)] and it is higher than that of the inverter without waveform control which is $v_{c1 \max} = v_{c2 \max} = 213 + 77.75 = 290.75$ V [see Fig. 5(b)]. Hence, the voltage stress on the power components is higher with waveform control than without waveform control.

The maximum inductor current of the inverter with waveform control is $i_{L1 \max} = i_{L2 \max} = 6.37$ A [see Fig. 5(f)] and it is lower than that of the inverter without waveform control which is $i_{L1 \max} = i_{L2 \max} = 7.18$ A [see Fig. 5(c)]. Hence, the current stress on the power components is lower with the waveform control than without waveform control. Additionally, the inductor current waveform is more symmetrical with the waveform control and this allows the full utilization of the bidirectional current capacity of the switch. According to (11), (12), (18), and (19), the relationship of V_d , B , and $v_{c \max}$ and the relationship of V_d , B , and $i_{L \max}$ can be shown in Fig. 6(a) and (b), respectively. From the figures, we can see that the voltage and current stresses increase with a decreasing B and an increasing V_d . The point $V_d = 213$ V, $B = 43$ V, $v_{c \max} = 314$ V given in Fig. 6(a) and the point $V_d = 213$ V, $B = 43$ V, $i_{L \max} = 6.37$ A given in Fig. 6(b) match the point in Fig. 4 when $C = 15$ μ F. Therefore, to reduce the voltage and current stresses of all power components in the topology, a large B and a small V_d is suggested.

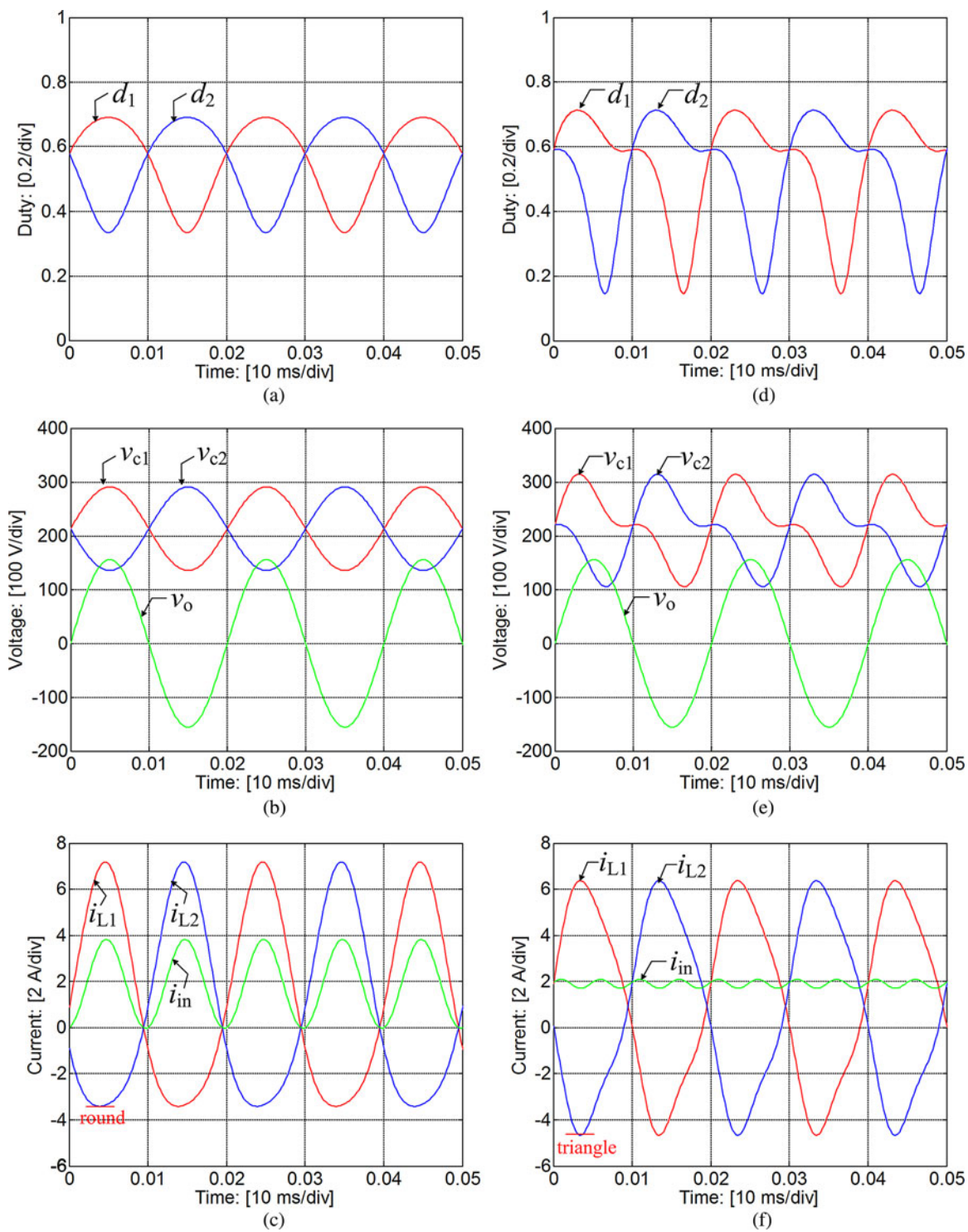


Fig. 5. Duty cycle, voltage, and current waveforms of the boost differential inverter (a)–(c) without waveform control and (d)–(f) with waveform control. (a) The duty cycle waveform without waveform control method. (b) The voltage waveform without waveform control method. (c) The current waveform without waveform control method. (d) The duty cycle waveform with the proposed method. (e) The voltage waveform with the proposed method. (f) The current waveform with the proposed method.

C. Flow Path of a Double-Line-Frequency Current Component

The flow path of the double-line-frequency current in the power circuit can have a significant impact on the power efficiency and it must be carefully studied. By substituting (23) and

(24) into (18) and (19), we have

$$i_{L1w} = I_D + A_{ww} \sin(\omega t + \theta_1) + A_{3ww} \sin(3\omega t + \theta_3) + A_{4ww} \sin(4\omega t + \theta_4) \quad (25)$$

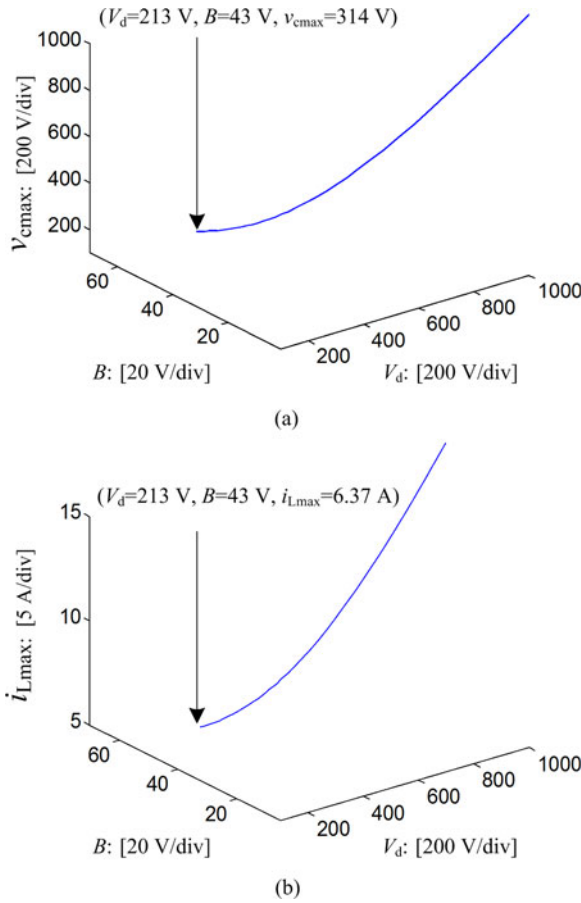


Fig. 6. Plot of the relationship of V_d , B and (a) $v_{c\max}$ and (b) $i_{L\max}$.

and

$$i_{L2w} = I_D - A_{3ww} \sin(3\omega t + \theta_3) + A_{4ww} \sin(4\omega t + \theta_4) \quad (26)$$

where i_{L1w} and i_{L2w} are the inductor currents of the inverter with the proposed waveform control, I_D is the dc component of these currents, and the coefficients A_{ww} , A_{3ww} , and A_{4ww} are the amplitudes of the fundamental and harmonic components of these currents, and they can be expressed as shown in (27)–(29), at the bottom of this page.

By inspecting the ac components of (14), (15), (25), and (26), it is clearly found that with waveform control, the double-line-frequency current component flows mainly through capacitors C_1 and C_2 , and has an insignificant flow through inductors L_1 and L_2 . This is graphically depicted in Fig. 7(a).

On the other hand, without waveform control [20], [21], the expressions of the inductors currents can be derived as

$$i_{L1t} = I_D + A_{wt} \sin(\omega t + \varphi_1) + A_{2wt} \sin(2\omega t + \varphi_2) \quad (30)$$

and

$$i_{L2t} = I_D - A_{wt} \sin(\omega t + \varphi_1) + A_{2wt} \sin(2\omega t + \varphi_2) \quad (31)$$

where the coefficients A_{wt} and A_{2wt} are the amplitudes of the fundamental and harmonic components of the inductor currents, and they can be expressed as

$$A_{wt} = \frac{V_d}{V_{in}} \sqrt{(\omega C V_{\max}/2)^2 + (I_{\max})^2} \quad (32)$$

$$A_{2wt} = \frac{\sqrt{(\omega C V_{\max}^2/8)^2 + (V_{\max} I_{\max}/4)^2}}{V_{in}} \quad (33)$$

From (1) and (2), the expressions of the capacitor currents without waveform control can be derived as

$$i_{c1t} = C\omega \frac{1}{2} V_{\max} \cos(\omega t) \quad (34)$$

and

$$i_{c2t} = -C\omega \frac{1}{2} V_{\max} \cos(\omega t). \quad (35)$$

Equations (30), (31), (34), and (35) clearly show that the double-line-frequency current component will mainly flow through L_1 and L_2 instead of C_1 and C_2 , as depicted in Fig. 7(b).

Since the inductor is usually a more lossy device (comprising core loss and a higher conductive loss) as compared to the capacitor, it is justify to conclude that the current flow path of the double-line-frequency current given in Fig. 7(b) is more power dissipative than that in Fig. 7(a). Such a conclusion is further verified by the circuit-simulation results given in Fig. 8, which shows the amplitudes of the double-line-frequency current component flowing through each of the main circuit components. From the figure, it is shown that with waveform control, the double-line-frequency current component will mainly flow through C_1 , C_2 , T_1 , T_2 , T_3 , and T_4 whereas without waveform control, the double-line-frequency current component will mainly flow through T_1 , T_3 , L_1 , L_2 , and the fuel cell. This coincides with the theoretical deduction illustrated in Fig. 7. Besides, the double-line-frequency current component flowing through T_1 , T_2 , T_3 , and T_4 will be more balanced with waveform control than that without waveform control.

$$A_{ww} = \sqrt{\frac{V_{\max}^6 \omega^2 C^2}{4096 V_d^2 V_{in}^2} + \frac{31 V_{\max}^4 I_{\max}^2}{512 V_d^2 V_{in}^2} - \frac{V_{\max}^3 \omega^2 C^2}{64 V_{in}^2} - \frac{7 V_{\max}^2 I_{\max}^2}{16 V_{in}^2} + \frac{V_{\max}^2 I_{\max}^4}{16 \omega^2 C^2 V_d^2 V_{in}^2} + \frac{\omega^2 C^2 V_d^2 V_{\max}^2}{4 V_{in}^2} + \frac{V_d I_{\max}^2}{V_{in}^2}} \quad (27)$$

$$A_{3ww} = \frac{V_{\max}}{8 V_d V_{in}} \sqrt{\frac{5 V_{\max}^2 I_{\max}^2}{8} + \frac{9 V_{\max}^4 \omega^2 C^2}{64} + \frac{I_{\max}^4}{4 \omega^2 C^2}} \quad (28)$$

$$A_{4ww} = \frac{V_{\max}^2 I_{\max}^2}{64 \omega C V_d^2 V_{in}} + \frac{V_{\max}^4 \omega C}{256 V_d^2 V_{in}} \quad (29)$$

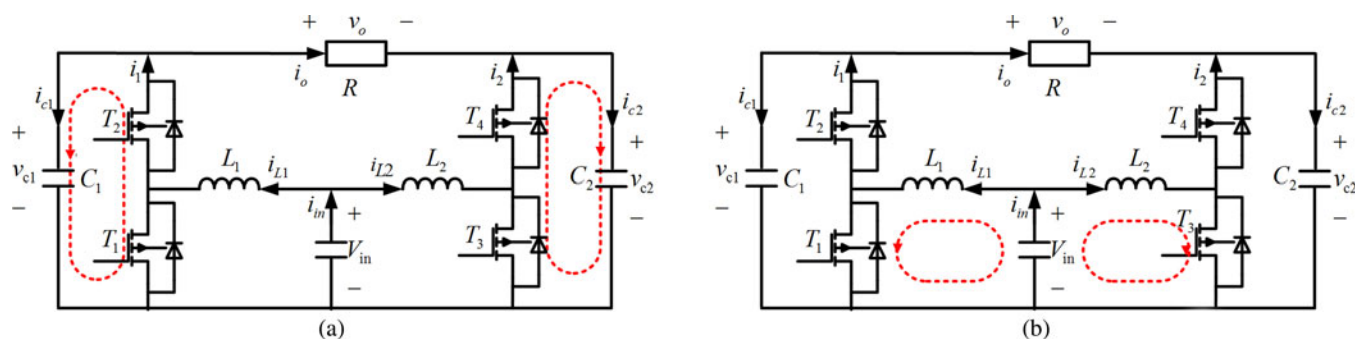


Fig. 7. Flow path of the double-line-frequency current component of the inverter. (a) With waveform control. (b) Without waveform control.

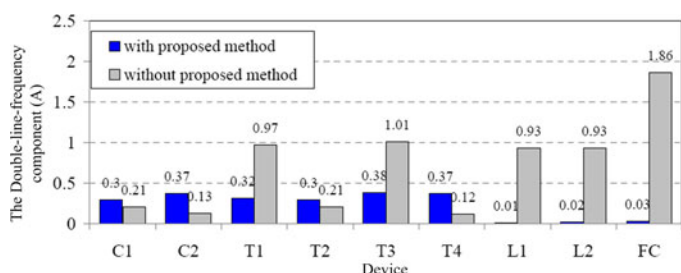


Fig. 8. Amplitude of a double-line-frequency current component on the respective power devices.

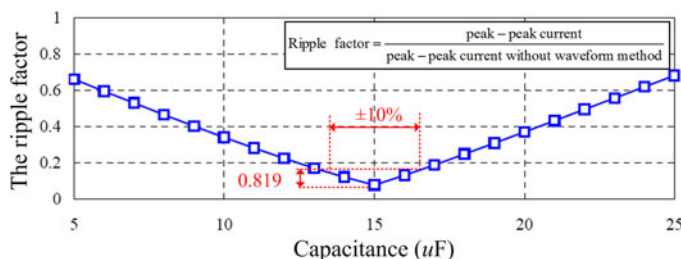


Fig. 9. Double-line-frequency current ripple factor versus capacitance of the inverter with waveform control designed under the assumption that $C_1 = C_2 = 15 \mu\text{F}$.

D. Effect of Capacitance Tolerance

Since the values of the capacitors C_1 and C_2 can affect the computation of the proposed waveform control, the effect of using a difference capacitance from that originally assumed in the computation on the control performance must be investigated. First, the parameters C_1 and C_2 in (23) and (24) are chosen as $C_1 = C_2 = 15 \mu\text{F}$ for the voltage reference calculation adopted in waveform control. Then, a circuit simulation with C_1 and C_2 in the power stage varying from 5 to 25 μF is performed. The simulated results are given in Fig. 9. It is observed that a larger deviation of the capacitor value from the assumed value of 15 μF leads to a poorer compensation of the double-line-frequency component. Yet, as the tolerance of the film capacitor is usually less than 10%, the effect of capacitance tolerance on the compensation capability is small (less than 8.19%), as given in Fig. 9.

E. Further Remarks

The adoption of the proposed waveform control method to mitigate the low-frequency input current ripple will alter the original behavior of the differential inverter without waveform control. The following are important points to consider in terms of the adoption of waveform control:

- 1) there is no change in the desired ac output voltage even though the voltages of the capacitors themselves are altered;
- 2) the energy stored by the capacitors, which is a function of the voltages, is made up of a dc component and a double-line-frequency component;
- 3) DC energy is stored by the two capacitors while they supply ac energy to the output load. Consequently, the low-frequency power pulsation caused by ac output is absorbed by the capacitors while the fuel cells kept a constant supply of dc power to the capacitors;
- 4) as the capacitor voltages v_{c1} and v_{c2} are much higher than the dc input voltage v_{in} , the energy transfer will occur when the voltage fluctuation on C_1 and C_2 is increased.

An interesting point to take note is that since the capacitor voltages can be large without affecting the desired ac output voltage, both capacitors can be minimized without increasing the ripple voltage on the dc input. The advantage is that film capacitors can be used instead of electrolytic capacitors to improve reliability. The practical limit is the voltage rating of the capacitors.

Another important point is that with the use of differential inverter, one may take an issue with the fuel cell having a floating ground that is in common with the high-frequency differential inverter [20], [21]. Note that as the output voltage of most fuel cells is relatively low as compared to the ac output requirement, there is no requirement for the fuel cell's output be grounded to the earth. However, if the metallic part of the fuel-cell system is exposed, then such a requirement is present [32]. In the case of differential inverters being used in applications where the ac output is connected to a single load, the fuel cell can be directly grounded to the earth, if necessary. On the other hand, as the output voltage of most fuel cells is relatively low as compared to the ac output requirement, it is typically necessary to include an isolated front-end boost stage before the differential inverter. In this case, the fuel cell can also be grounded to the earth, if needed.

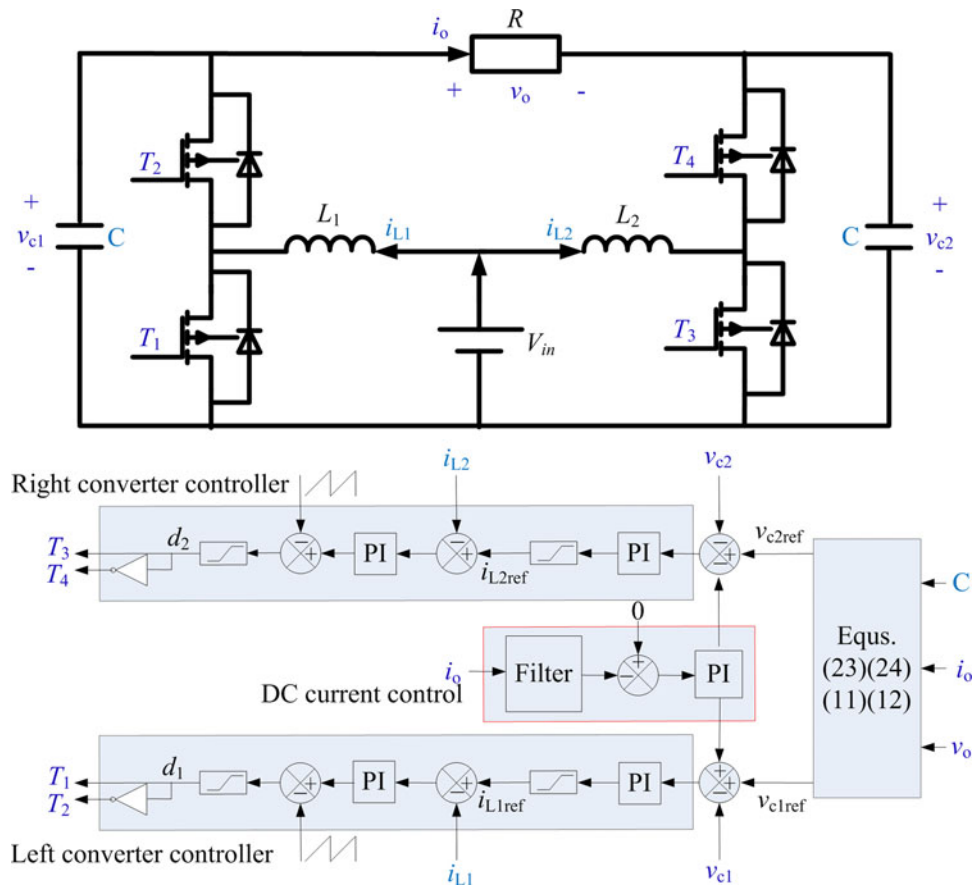


Fig. 10. Overview of the control block diagram of the differential inverter.

TABLE I
SPECIFICATIONS OF A BOOST DIFFERENTIAL INVERTER

Input voltage V_{in}	90 V
Output voltage (RMS)	110 V
Rated power P_e	170 W
Fundamental frequency f	50 Hz
Switch frequency f_s	20 kHz
Inductors (L_1, L_2)	300 μ H, 10 A
Capacitors (C_1, C_2)	15 μ F, 800 V, film cap.

V. EXPERIMENTAL RESULTS AND DISCUSSIONS

A. Control Block and Experimental Setup

To validate the proposed waveform control method, the boost differential inverter prototype as shown in Fig. 3 was implemented. The specifications of the prototype are given in Table I. The control platform is implemented using TMS320LF2812.

In this study, the boost inverter is based on a dual-loop control, of which each boost converter is controlled by means of an inner inductor current control loop and an outer output voltage control loop. An overview of the control block is shown in Fig. 10. Both control loops are designed using the averaged continuous-time model of the boost converter topology.

The principle of the control mechanism is as follows. First, the ac output voltage reference is split into the two respective voltage references v_{c1ref} and v_{c2ref} of the two boost converters as given in (23) and (24). The references v_{c1ref} and v_{c2ref} are compared with the feedback voltages v_{c1} and v_{c2} of the converters and fed into a proportional-integral (PI) (outer-loop) compensator, which generates the reference currents i_{L1ref} and i_{L2ref} for the inductor current control. These current references are compared with the feedback currents of the inductors L_1 and L_2 and are fed into another PI (inner-loop) compensator, which is followed by a pulse-width modulator (PWM) to produce the desired duty cycles d_1 and d_2 . The duty cycles are controlled between 0.1 and 0.7 to generate the voltages as described in (3), (11), and (12). With this control, the inverter is capable of maintaining a stable and reliable operating condition by means of limiting the inductor current.

It is possible for the output of the differential inverter to contain a dc offset component due to control time delays and practical imperfections. Such an offset is prohibited and should be minimized when the inverter is to be connected to the grid [33]. In this work, the dc offset voltage compensation loop is included in the control, as shown in the control block given in Fig. 10. By introducing a dc current control loop into the controlled system, the dc offset voltage of the output will be regulated to zero. The control block diagram in Fig. 10 including

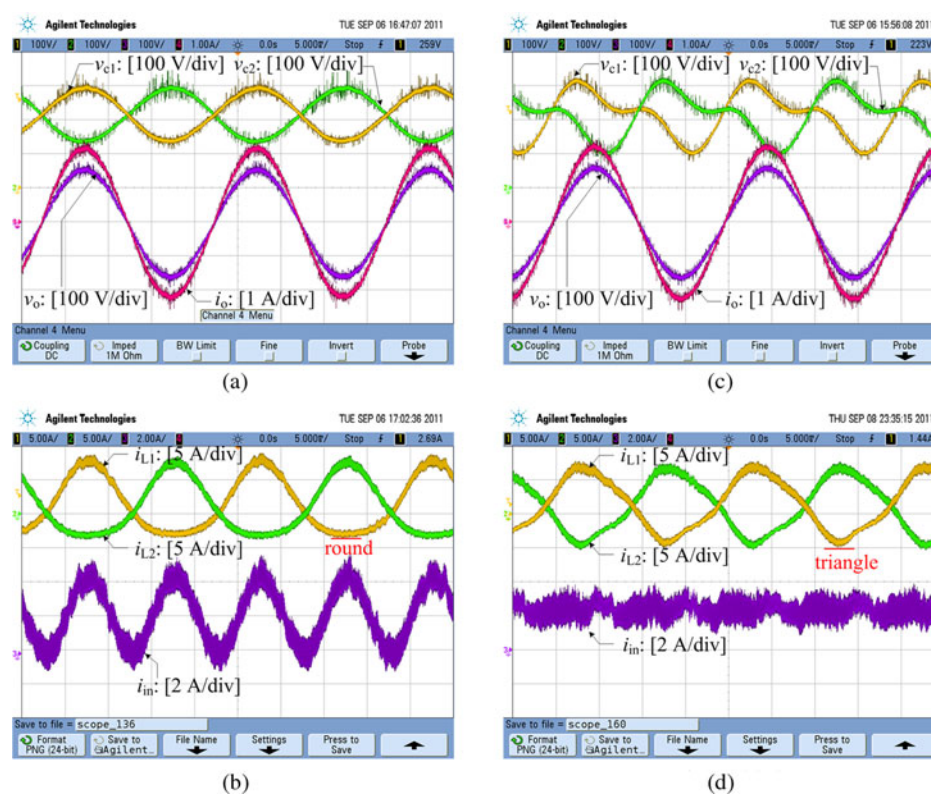


Fig. 11. Voltage and current waveforms of the inverter under a pure resistive load ($R = 70.5 \Omega$). (a) The voltage waveform without waveform control method. (b) The current waveform without waveform control method. (c) The voltage waveform with the proposed method. (d) The current waveform with the proposed method.

the digital PI controller is implemented using the DSP unit TMS320LF2812.

B. Under a Resistive Load

Fig. 11(a)–(d) shows the voltage and current waveforms of the boost inverter operating at rated power under a pure resistive R load for both cases of with and without waveform control. Fig. 11(a) and (c) shows the waveforms of the capacitor voltages, output voltage, and load current of the inverter, respectively, without waveform control and with waveform control. It is illustrated that the same output voltage and load current can be obtained from both control methods even though the capacitor voltages are different. Fig. 11(b) and (d) shows the waveforms of the inductor current and the input current of the inverter, respectively, without waveform control and with waveform control. It is illustrated that with the proposed waveform control method, the input current ripple is mitigated to a magnitude of less than 13% (from 4 to 0.5 A) of the ripple obtained without waveform control.

Fig. 12(a) and (b) shows, respectively, the frequency spectrum characteristic of the input current of the inverter without waveform control and with waveform control. For the case of no waveform control, the 100 Hz current ripple (amplitude of 1.11 A) is 48.1% of dc current (2.31 A). However, for the case of waveform control, the 100 Hz current ripple (amplitude of 0.07 A) is only 3% of dc current (2.37 A), which is well within the limits suggested in [9]. The 200 Hz current ripple of the

inverter without waveform control is 1.1% of dc current (amplitude of 0.026 A) and with waveform control is 5% of dc current (amplitude of 0.1176 A). However, this has only negligible effect on the fuel cells.

Fig. 12(c) and (d) shows, respectively, the frequency spectrum characteristic of the output voltage of the inverter without waveform control and with the waveform control. Here, the total harmonic distortion (THD) of the output voltage of the inverter without waveform control is 1.089% and with waveform control is 2.36%. Both are within the limit of the ac grid requirements [34].

C. Under a Resistive-Capacitive Load

To further show the validity of the proposed method, other load conditions are tested. Here, RC load is chosen.

Fig. 13(a)–(d) shows the voltage and current waveforms of the boost inverter operating at rated power under a resistive-capacitive RC load. Fig. 13(a) and (c) shows, respectively, the waveforms of the capacitor voltages, output voltage, and load current of the inverter without waveform control and with waveform control. It is illustrated that the same output voltage and load current can be obtained from both control methods even though the capacitor voltages are different. Fig. 13(b) and (d) shows, respectively, the waveforms of the inductor current and the input current of the inverter without waveform control and with waveform control. It is illustrated that with the proposed waveform control method, the input current ripple is mitigated

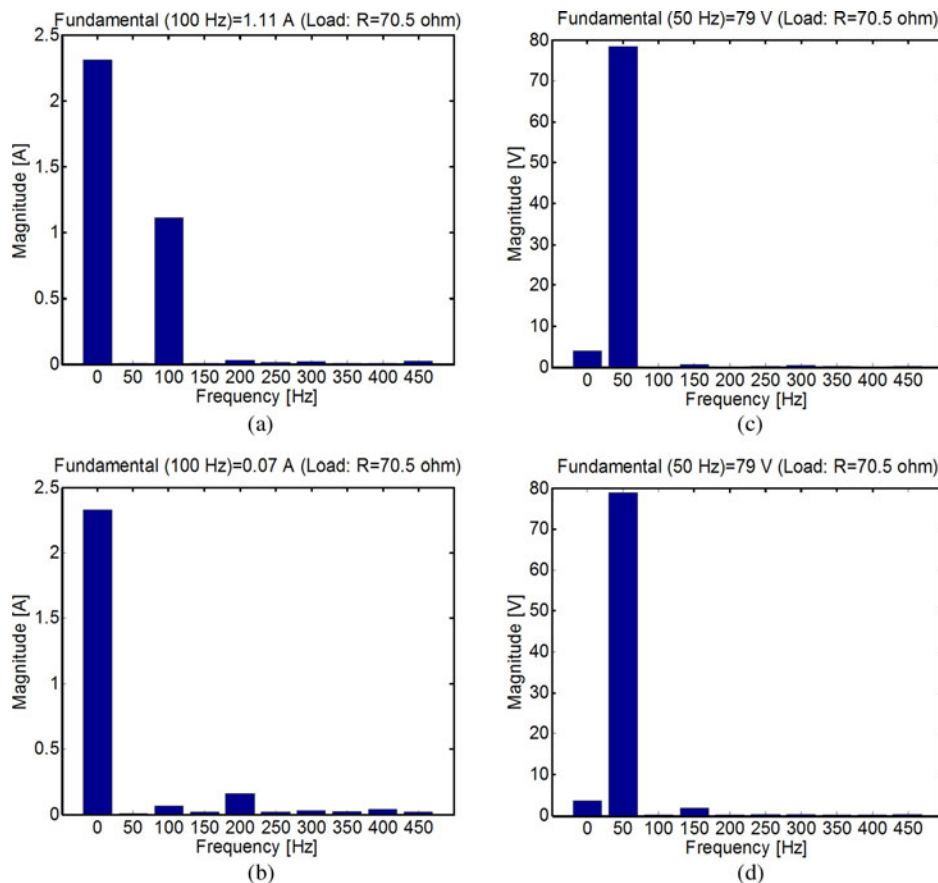


Fig. 12. Input current and output voltage frequency characteristics under pure resistive load ($R = 70.5 \Omega$). (a) Input current without waveform method. (b) Input current with the proposed method. (c) Output voltage without waveform method. (d) Output voltage with the proposed method.

to a magnitude of less than 40% (from 4 to 1.6 A) of the ripple that is obtained without waveform control.

Fig. 14(a) and (b) shows, respectively, the frequency spectrum characteristic of the input current of the inverter without waveform control and with waveform control. For the case of no waveform control, the 100 Hz current ripple (amplitude of 1.01 A) is 55.4% of dc current (1.82 A). However, for the case of with waveform control, the 100 Hz current ripple (amplitude of 0.22 A) is only 11.9% of dc current (1.84 A), which is well within the limits suggested in [9]. The 200 Hz current ripple of the inverter without waveform control is 0.79% of dc current (amplitude of 0.015 A) and with waveform control is 8.9% of dc current (amplitude of 0.1647 A). This has negligible effect on the fuel cells.

Fig. 14(c) and (d) shows, respectively, the frequency spectrum characteristic of the output voltage of the inverter without waveform control and with waveform control. Here, the THD of output voltage of the inverter without waveform control is 0.69% and with waveform control is 2.55%, which are within the limit [34].

D. Comparative Study of Waveform Control Versus No Waveform Control With Circuit Modification

As mentioned, without waveform control, the double-line-frequency current component will not flow through capacitors

C_1 and C_2 . Therefore, a change in their capacitance values will not affect the current ripple. Consequently, the mitigation of the double-line-frequency component of the input current of the inverter without waveform control can be achieved only through the application of an extra device (e.g., by inserting an input capacitor to the inverter) or the use of an auxiliary converter that can alter the flow path of this component.

In this section, a comparative study on the addition of an input capacitor to the inverter without waveform control as compared to the use of waveform control is performed. Here, the double-line-frequency ripple levels under various configurations are performed. With the same capacitances $C_1 = C_2 = 15 \mu\text{F}$ and the same load ($R = 70.5 \Omega$), the output voltage and input current waveform of the inverter for four separate cases are given in Fig. 15. The configurations of the four cases are as follows— Case I: without waveform control (no input capacitor); Case II: without waveform control but with 220 μF input electrolytic capacitor; Case III: without waveform control but with 2240 μF input electrolytic capacitor; Case IV: with proposed waveform control (no input capacitor).

From Fig. 15, it is shown that the output voltage v_o can be controlled as sinusoidal; however, the peak-to-peak (double-line-frequency component) of the input current is, respectively, 4, 3.8, 3.4, and 0.5 A in the four cases. With the same set of C_1 and C_2 values, the use of the proposed waveform control method produces the minimal current ripple. The input current

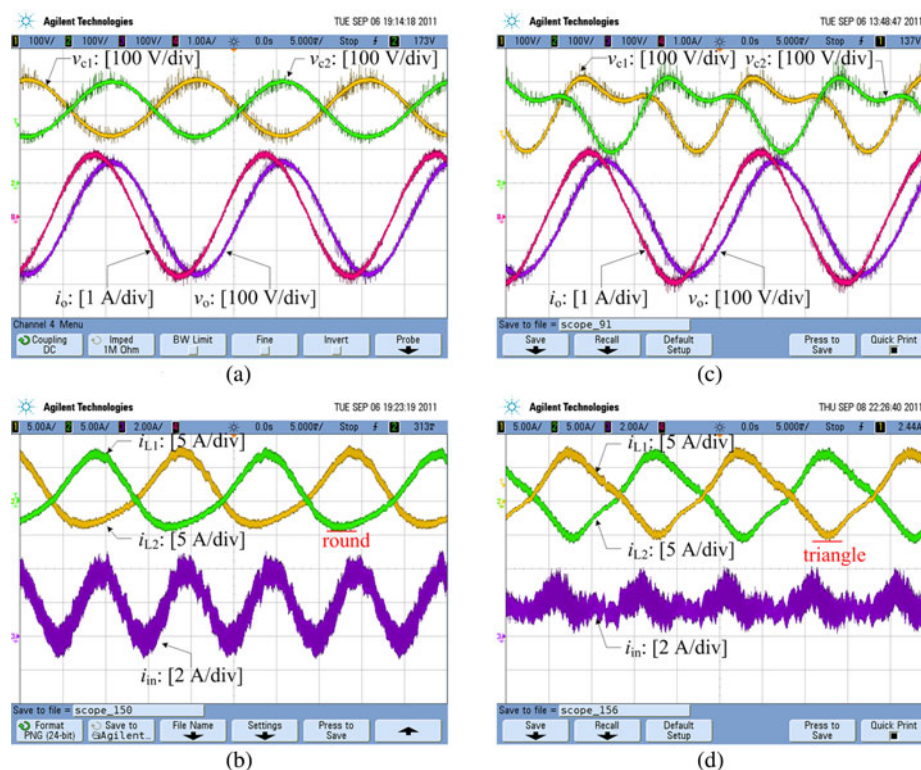


Fig. 13. Voltage and current waveforms of the inverter under a resistive-capacitive load ($R = 70.5 \Omega$, $C = 65 \mu F$). (a) The voltage waveform without waveform control method. (b) The current waveform without waveform control method. (c) The voltage waveform with the proposed method. (d) The current waveform with the proposed method.

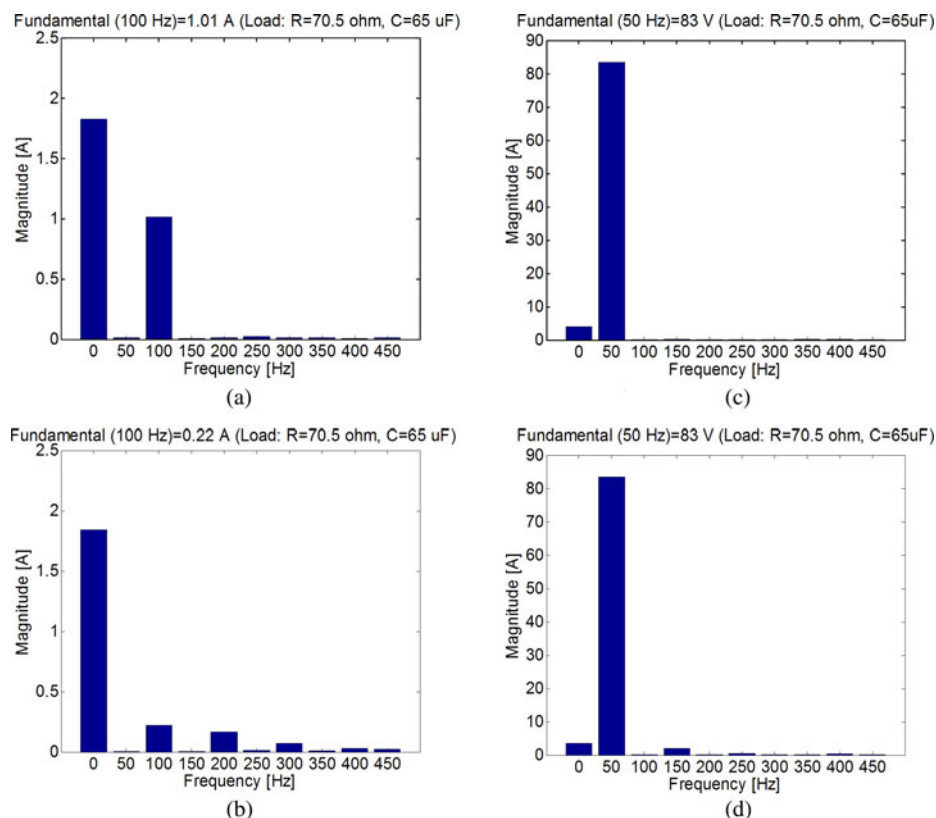


Fig. 14. Input current and output voltage frequency characteristics under resistive-capacitive load ($R = 70.5 \Omega$, $C = 65 \mu F$). (a) Input current without waveform method. (b) Input current with the proposed method. (c) Output voltage without waveform method. (d) Output voltage with the proposed method.

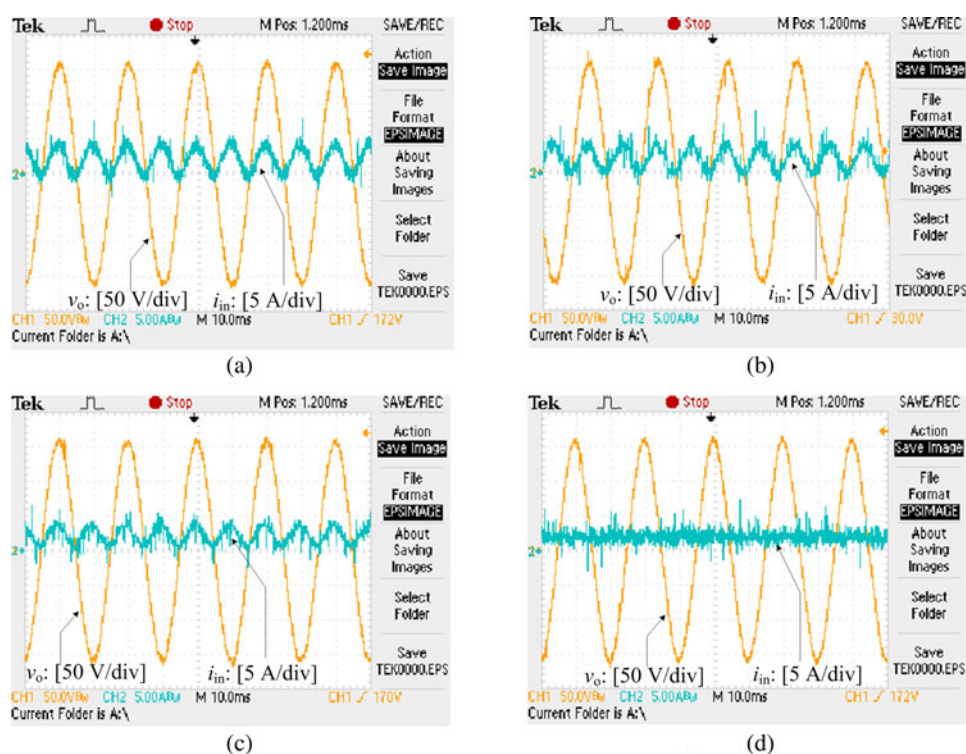


Fig. 15. Input current waveform in four cases. (a) Case I: without waveform control; (b) Case II: without waveform control but with a 220 μF input capacitor; (c) Case III: without waveform control but with a 2240 μF input capacitor; and (d) Case IV: with waveform control.

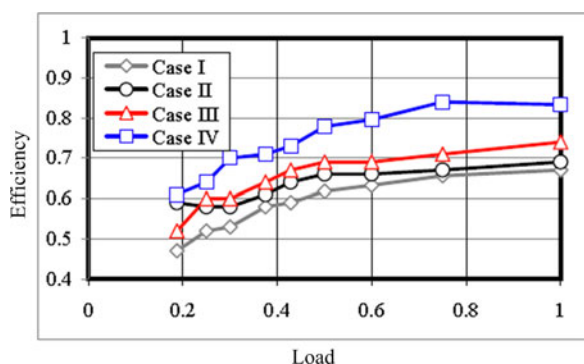


Fig. 16. The efficiency curves of the four cases. (a) Case I: without waveform control; (b) Case II: without waveform control but with a 220 μF input capacitor; (c) Case III: without waveform control but with a 2240 μF input capacitor; and (d) Case IV: with waveform control.

ripple is mitigated to a magnitude of less than 13% (from 4 to 0.5 A) of the ripple magnitude that is obtained for the case of without waveform control (Case I). Additionally, without waveform control, the use of an input capacitor can help in suppressing the current ripple. However, the effect is not obvious and a very large electrolytic capacitor will be needed to achieve significant suppression.

Finally, the circuit efficiency curves for the four respective configuration obtained experimentally are given in Fig. 16. From Fig. 16, it can be seen that power efficiency is higher with waveform control than without waveform control.

VI. CONCLUSION

A waveform control method for mitigating low-frequency current ripple in fuel-cell inverter systems is proposed in this paper. The mechanism of the proposed method is analyzed, discussed, and experimentally verified. It is shown that with the proposed method, the low-frequency power pulsation caused by ac output is absorbed by the capacitors while the fuel cells kept a constant supply of dc power to the capacitors, thereby eliminating the effect of low-frequency ripple from affecting the properties of fuel cells. Since capacitor voltages can be large without affecting the desired ac output voltage, capacitors of the inverter can be minimized. This allows the use of film capacitors over electrolytic capacitors, thereby improving the inverter's lifetime. The proposed method is applicable in systems where current ripple mitigation is required, such as for the purpose of eliminating electrolytic capacitor in PV and LED systems.

ACKNOWLEDGMENT

The authors would like to thank Dr. S. C. Wong for many stimulating discussions and K. W. Wang for his technical support.

REFERENCES

- [1] C. Liu and J. S. Lai, "Low frequency current ripple reduction technique with active control in a fuel cell power system with inverter load," *IEEE Trans. Power Electron.*, vol. 22, no. 4, pp. 1429–1436, Jul. 2007.
- [2] W. Choi, P. N. Enjeti, and J. W. Howze, "Development of an equivalent circuit model of a fuel cell to evaluate the effects of inverter ripple current," in *Proc. IEEE Appl. Power Electron. Conf.*, Feb. 2004, pp. 355–361.

- [3] S. Pradhan, S. K. Mazumder, J. Hartvigsen, and M. Hollist, "Effects of electrical feedbacks on planar solid-oxide fuel cell," *Trans. ASME, J. Fuel Cell Sci. Tech.*, vol. 4, no. 2, pp. 154–166, May 2007.
- [4] J. F. Wu, X. Z. Yuan, J. J. Martin, H. J. Wang, J. J. Zhang, J. Shen, S. H. Wu, and W. Merida, "A review of PEM fuel cell durability: Degradation mechanisms and mitigation strategies," *J. Power Sources*, vol. 184, pp. 104–119, Jun. 2008.
- [5] J. H. Kim, M. H. Jang, J. S. Choe, D. Y. Kim, Y. S. Tak, and B. H. Cho, "An experimental analysis of the ripple current applied variable frequency characteristic in a polymer electrolyte membrane fuel cell," *J. Power Electron.*, vol. 11, no. 1, Jan. 2011.
- [6] R. S. Gemmen, "Analysis for the effect of inverter ripple current on fuel cell operating condition," *J. Fluids Eng.*, vol. 125, no. 3, pp. 576–585, May 2003.
- [7] J. S. Kim, G. Y. Choe, H. S. Kang, and B. K. Lee, "Robust low frequency current ripple elimination algorithm for grid-connected fuel cell systems with power balancing technique," *Renew. Energy*, vol. 36, pp. 1392–1400, 2011.
- [8] G. Fontes, C. Turpin, S. Astier, and T. A. Meynard, "Interactions between fuel cells and power converters: Influence of current harmonics on a fuel cell stack," *IEEE Trans. Power Electron.*, vol. 22, no. 2, pp. 670–678, Mar. 2007.
- [9] EG&G Technical Service Inc. *Fuel Cell Handbook*, 7th ed. U.S. Department of Energy, ch. 8, 2004.
- [10] Nexa™ (310-0027) *Power Module User's Manual*, Ballard Power Systems Inc., BC, Canada, 2003.
- [11] M. Schenck, J. S. Lai, and K. Stanton, "Fuel cell and power conditioning system interactions," in *Proc. IEEE Appl. Power Electron. Conf.*, Jun. 2005, vol. 1, pp. 114–120.
- [12] T. Shimizu, K. Wada, and N. Nakamura, "Flyback-type single-phase utility interactive inverter with power pulsation decoupling on the DC input for an AC photovoltaic module system," *IEEE Trans. Power Electron.*, vol. 21, no. 5, pp. 1264–1272, Sep. 2006.
- [13] S. K. Mazumder, R. K. Burra, and K. Acharya, "A ripple-mitigating and energy-efficient fuel cell power-conditioning system," *IEEE Trans. Power Electron.*, vol. 22, no. 4, pp. 1437–1452, Jul. 2007.
- [14] J. I. Itoh and F. Hayashi, "Ripple current reduction of a fuel cell for a single-phase isolated converter using a DC active filter with a center tap," *IEEE Trans. Power Electron.*, vol. 25, no. 3, pp. 550–556, Mar. 2010.
- [15] A. Testa, S. D. Caro, and D. Caniglia, "Compensation of the low frequency current ripple in single phase grid connected fuel cell power systems," in *Proc. Eur. Conf. Power Electron. Appl.*, 2009, pp. 1–10.
- [16] X. Li, W. P. Zhang, H. Li, R. Xie, M. Chen, G. Q. Shen, and D. H. Xu, "Power management unit with its control for a three-phase fuel cell power system without large electrolytic capacitors," *IEEE Trans. Power Electron.*, vol. 26, no. 12, pp. 3766–3777, Dec. 2011.
- [17] J. M. Kwon, E. H. Kim, B. H. Kwon, and K. H. Nam, "High-efficiency fuel cell power conditioning system with input current ripple reduction," *IEEE Trans. Ind. Electron.*, vol. 56, no. 3, pp. 826–834, Mar. 2009.
- [18] R. J. Wai and C. Y. Lin, "Dual active low frequency ripple control for clean energy power conditioning mechanism," *IEEE Trans. Ind. Electron.*, vol. 58, no. 11, pp. 5172–5185, Nov. 2011.
- [19] Y. J. Song and P. N. Enjeti, "A high frequency link direct DC-AC converter for residential fuel cell power systems," in *Proc. IEEE Power Electron. Spec. Conf.*, 2004, pp. 4755–4761.
- [20] M. Jang and V. G. Agelidis, "A minimum power-processing stage fuel cell energy system based on a boost-inverter with a bi-directional back-up battery storage," *IEEE Trans. Power Electron.*, vol. 26, no. 5, pp. 1568–1577, Dec. 2011.
- [21] M. Jang, M. Ciobotaru, and V. G. Agelidis, "A single-stage fuel cell energy system based on a buck-boost inverter with a backup energy storage unit," *IEEE Trans. Power Electron.*, vol. 27, no. 6, pp. 2825–2834, Dec. 2012.
- [22] Y. J. Song, S. B. Han, X. Li, S. I. Park, H. G. Jeong, and B. M. Jung, "A power control scheme to improve the performance of a fuel cell hybrid power source for residential application," in *Proc. IEEE Power Electron. Spec. Conf.*, 2007, pp. 1261–1266.
- [23] R. O. Cáceres and I. Barbi, "A boost DC/AC converter: Analysis, design, and experimentation," *IEEE Trans. Power Electron.*, vol. 14, no. 1, pp. 134–141, Jan. 1999.
- [24] P. Sanchis, A. Ursaea, E. Gubia, and L. Marroyo, "Boost DC/AC inverter: A new control strategy," *IEEE Trans. Power Electron.*, vol. 20, no. 2, pp. 343–353, Mar. 2005.
- [25] R. O. Cáceres, W. M. Garcia, and O. E. Camacho, "A buck boost DC-AC converter: Operation, analysis, and control," in *Proc. Int. Power Electron. Conf.*, 1998, pp. 126–131.
- [26] J. Almazan, N. Vazquez, C. Hernandez, J. Alvarez, and J. Arau, "A comparison between the buck, boost and buck-boost inverters," in *Proc. IEEE Int. Power Electron. Conf.*, 2000, pp. 341–346.
- [27] S. K. Mazumder, R. K. Burra, R. Huang, and V. Arguelles, "A low-cost single-stage isolated differential Cúk inverter for fuel-cell application," in *Proc. IEEE Power Electron. Spec. Conf.*, 2008, pp. 4426–4431.
- [28] L. Sun, Y. Liang, C. Gong, and Y. Yan, "Research on single-stage flyback inverter," in *Proc. IEEE Power Electron. Spec. Conf.*, 2005, pp. 849–854.
- [29] Y. Ma, B. Qiu, and Q. Cong, "Research on single-stage inverter based on bi-directional Buck DC converter," in *Proc. IEEE Power Electron. Distributed Generation Syst.*, 2010, pp. 299–303.
- [30] Z. Yan, J. Li, W. Zhang, Q. Zhang, Y. Zheng, and W. Wu, "Topology family and the simulation of "BOOK" differential single stage inverter," in *Proc. IEEE Power Electron. Distributed Generation Syst.*, 2010, pp. 204–209.
- [31] N. Vázquez, J. Alvarez, C. Aguilar, and J. Arau, "Some critical aspects in sliding mode control design for the boost inverter," in *Proc. IEEE Int. Power Electron. Conf.*, 1998, pp. 76–81.
- [32] Energy Safe Victoria, "Installation & inspection of fuel cells," Guidance Notes, May 2011.
- [33] M. Armstrong, D. J. Atkinson, C. M. Johnson, and T. D. Abeyasekera, "Auto-calibrating DC link current sensing technique for transformerless, grid connected, H-bridge inverter systems," *IEEE Trans. Power Electron.*, vol. 21, no. 5, pp. 1385–1393, Sep. 2006.
- [34] F. Blaabjerg, Z. Chen, and S. B. Kjaer, "Power electronics as efficient interface in dispersed power generation systems," *IEEE Trans. Power Electron.*, vol. 19, no. 5, pp. 1184–1194, Sep. 2004.



Guo-Rong Zhu (M'11) was born in Hunan, China. She received the Ph.D. degrees in electrical engineering from the Huazhong University of Science and Technology, Wuhan, China, in 2009.

From 2002 to 2005, she was a Lecturer at the School of Electrical Engineering, Wuhan University of Science and Technology, Wuhan. From 2009 to 2011, she was a Research Assistant/Research Associate in the Department of Electronic and Information Engineering, the Hong Kong Polytechnic University, Kowloon, Hong Kong. She is currently an Associate Professor at the School of Automation, Wuhan University of Technology, Wuhan. Her main research interests include soft-switching dc/dc converters, inverters, battery management system of hybrid electric vehicles, and renewable energy system.



Siew-Chong Tan (S'00–M'06–SM'11) received the B.Eng. (Hons.) and M.Eng. degrees in electrical and computer engineering from the National University of Singapore, Singapore, in 2000 and 2002, respectively, and the Ph.D. degree in electronic and information engineering from the Hong Kong Polytechnic University, Hung Hom, Kowloon, Hong Kong, in 2005.

From October 2005 to May 2012, he was a Research Associate, Postdoctoral Fellow, Lecturer, and Assistant Professor in the Department of Electronic and Information Engineering, Hong Kong Polytechnic University. From January to October 2011, he was a Senior Scientist in Agency for Science, Technology and Research (A*Star), Singapore. He is currently an Associate Professor in the Department of Electrical and Electronic Engineering, The University of Hong Kong, Pokfulam, Hong Kong. He was a Visiting Scholar at the Grainger Center for Electric Machinery and Electro mechanics, University of Illinois at Urbana-Champaign, Champaign, from September to October 2009, and an Invited Academic Visitor of Huazhong University of Science and Technology, Wuhan, China, in December 2011. He is a coauthor of the book *Sliding Mode Control of Switching Power Converters: Techniques and Implementation* (Boca Raton, FL: CRC Press, 2011). His research interests include power electronics and control, LED lightings, smart grids, and clean energy technologies.

Dr. Tan serves extensively as a Reviewer for various *IEEE/IET Transactions and Journals on Power, Electronics, Circuits, and Control Engineering*.



Yu Chen (S'09–M'11) received the B.E. and Ph.D. degrees in electrical and electronic engineering from the Huazhong University of Science and Technology, Wuhan, China, in 2006 and 2011, respectively.

From March 2008 to March 2009, he was an Intern in GE Global Research Center, Shanghai, China. In September 2011, he joined Huazhong University of Science and Technology, Wuhan, as a Lecturer. His research interests include the power electronic converter topologies, soft-switching techniques, converter modeling, the fault diagnosis techniques, and the wind energy power-conversion system.



Chi K. Tse (M'90–SM'97–F'06) received the B.Eng. (first class Hons.) degree in electrical engineering and the Ph.D. degree from the University of Melbourne, Melbourne, Australia, in 1987 and 1991, respectively.

He is currently the Chair Professor and Head of the Department of Electronic and Information Engineering at the Hong Kong Polytechnic University, Hung Hom, Kowloon, Hong Kong. He is the author of the books titled *Linear Circuit Analysis* (London, U.K.: Addison-Wesley, 1998) and *Complex Behavior of Switching Power Converters* (Boca Raton, FL:

CRC Press, 2003), and a coauthor of books titled *Chaos-Based Digital Communication Systems* (Heidelberg, Germany: Springer-Verlag, 2003), *Digital Communications with Chaos* (London: Elsevier, 2006), *Reconstruction of Chaotic Signal with Applications to Chaos-Based Communications* (Singapore: World Scientific, 2007), and *Sliding Mode Control of Switching Power Converters: Techniques and Implementation* (Boca Raton, FL: CRC Press, 2011). He is a coholder of four U.S. patents and two other pending patents. His research interests include complex network applications, power electronics, and chaos-based communications.

Dr. Tse currently serves as an Editor-in-Chief for the IEEE CIRCUITS AND SYSTEMS MAGAZINE and the IEEE CIRCUITS AND SYSTEMS SOCIETY NEWSLETTER. He was an Associate Editor for the IEEE TRANSACTIONS ON CIRCUITS AND SYSTEMS PART I, FUNDAMENTAL THEORY AND APPLICATIONS from 1999 to 2001 and again from 2007 to 2009. He has also been an Associate Editor for the IEEE TRANSACTIONS ON POWER ELECTRONICS since 1999. He is an Associate Editor of the *International Journal of Systems Science*, and also on the Editorial Board of the *International Journal of Circuit Theory and Applications* and *International Journal and Bifurcation and Chaos*. He also served as a Guest Editor and Guest Associate Editor for a number of special issues in various journals. In 2008, he was the Chairman of the Technical Committee on Nonlinear Circuits and Systems of the IEEE Circuits and Systems Society. He received the L.R. East Prize from the Institution of Engineers, Australia, in 1987, the Best Paper Award from the IEEE TRANSACTIONS ON POWER ELECTRONICS in 2001, and the Best Paper Award from the *International Journal of Circuit Theory and Applications* in 2003. In 2005 and 2011, he was selected and appointed as IEEE Distinguished Lecturer. In 2007, hereceived the Distinguished International Research Fellowship by the University of Calgary, Canada. In 2009, he and his coinventors received the Gold Medal with Jury's Commendation at the International Exhibition of Inventions of Geneva, Switzerland, for a novel driving technique for LEDs. In 2010, he was appointed the Chang Jiang Scholar Chair Professorship by the Ministry of Education of China and the appointment is hosted by Huazhong University of Science and Technology, Wuhan. In 2011, he was appointed Honorary Professor by RMIT University, Melbourne, Australia.